ADVANCED NANOBIOMED RESEARCH
Open Access
www.advnanobiomedres.com

Rotavirus Binding to Cell Surface Receptors Directly Recruiting α_2 Integrin

*Jinsung Yang, Jeongsoo Park, Melanie Koehler, Joshua Simpson, Daniel Luque, Javier M. Rodríguez, and David Alsteens**

Rotavirus interactions with endogenous cell surface receptors are of fundamental interest in virology and medicine; however, the evidence of rotavirus directly binding to the receptors and the consequent dynamic behaviors are still elusive. Force–distance curve-based atomic force microscopy allows for the extraction of biophysical properties underlying binding of single virions to receptors and clarification of the dynamics of rotavirus–receptor interactions. Unfortunately, this method is time-consuming due to the lack of automation when analyzing large data sets. Herein, rotavirus–receptor interactions and early endocytosis behaviors using automated high-throughput analysis are examined. It is demonstrated that rotavirus binds to α-linked sialic acid and $\alpha_2\beta_1$ integrin. The effect of trypsinization is investigated on the capsid protein VP4 binding to the receptors. Using fluidic force microscopy, it is demonstrated that the interaction leads to α_2 integrin recruitment to the cell-bound rotavirus on the plasma membrane. Further, it is illustrated that an integrin-derived peptide can impede binding and alter downstream dynamics. Taken together, these results open a new understanding of the infection mechanism of rotavirus and suggest a novel inhibitory peptide against rotavirus binding.

1. Introduction

Rotavirus infection was responsible for an estimated >125 000 young children (<5 years) deaths in 2016 throughout the world.[1] Although the number of deaths has halved since a vaccine became available in 2006, rotavirus infection was still responsible for about 30% of all diarrheal deaths among young children just 5 years ago.[1] Current vaccines are based on live-attenuated rotavirus containing one or multiple serotypes independently determined by the outer VP4 and VP7 proteins.[2] On virions, VP4 forms homotrimers projecting outward from the viral surface, made up of 260 trimers of VP7, and consist of two different domains: VP5* and VP8* (**Figure 1**A,B).[3] VP7 defines the glycosylated (G) genotype and VP4 establishes the protease sensitive (P). Currently, there are at least 51 P genotypes and 36 G genotypes. Despite the theoretical possibility for numerous rotavirus G/P reassortants, six account for 80–90% of circulating genotypes, namely, G1P[8], G2P[4], G3P[8], G4P[8], G9P[8], and G12P[8].[4] Some novel strains have recently emerged and continue to spread worldwide.[5] Therefore, a better understanding of the molecular mechanism underlying rotavirus infection as well as the development of specific antiviral agents is an urgent unmet need.

Central to virus infection is the translocation of virions through the cell membrane, allowing for downstream release of their genetic cargo. While internalization strategies vary between viruses, the initial step always involves the binding of viral proteins with one or multiple cell surface components, either attachment factors (e.g., surface glycans) and/or specific entry receptors. Several lines of evidence have demonstrated that rotaviruses interact sequentially with several cell surface molecules, using the virus surface proteins VP4 and VP7 (Figure 1A,B).[6] Upon the first contact, rotaviruses interact with glycans, for example, sialic acid (SA), through the region encompassed on the VP8* domain of VP4.[7–9] In addition to interactions with glycans, rotavirus can also engage heat shock cognate 71 kDa protein (hsc70)[10,11] and integrins via binding motifs present on either VP5* ($\alpha_2\beta_1$, $\alpha_4\beta_1$) or VP7 ($\alpha_V\beta_3$, $\alpha_x\beta_2$, $\alpha_4\beta_1$) (Figure 1B).[12–15] Recently, a new receptor for rotavirus, histoblood group antigen (HBGA), was discovered, indicating the need to better understand mechanisms associated with binding and entry.[16]

J. Yang, M. Koehler, J. Simpson, D. Alsteens
Louvain Institute of Biomolecular Science and Technology
Université Catholique de Louvain
Louvain-la-Neuve 1348, Belgium
E-mail: david.alsteens@uclouvain.be

J. Park
Cochlear.ai
Seoul 06103, South Korea

D. Luque
Centro Nacional de Microbiología/ISCIII
Madrid 28220, Spain

J. M. Rodríguez
Centro Nacional de Biotecnología/CSIC
Madrid 28049, Spain

The ORCID identification number(s) for the author(s) of this article can be found under https://doi.org/10.1002/anbr.202100077.

DOI: 10.1002/anbr.202100077

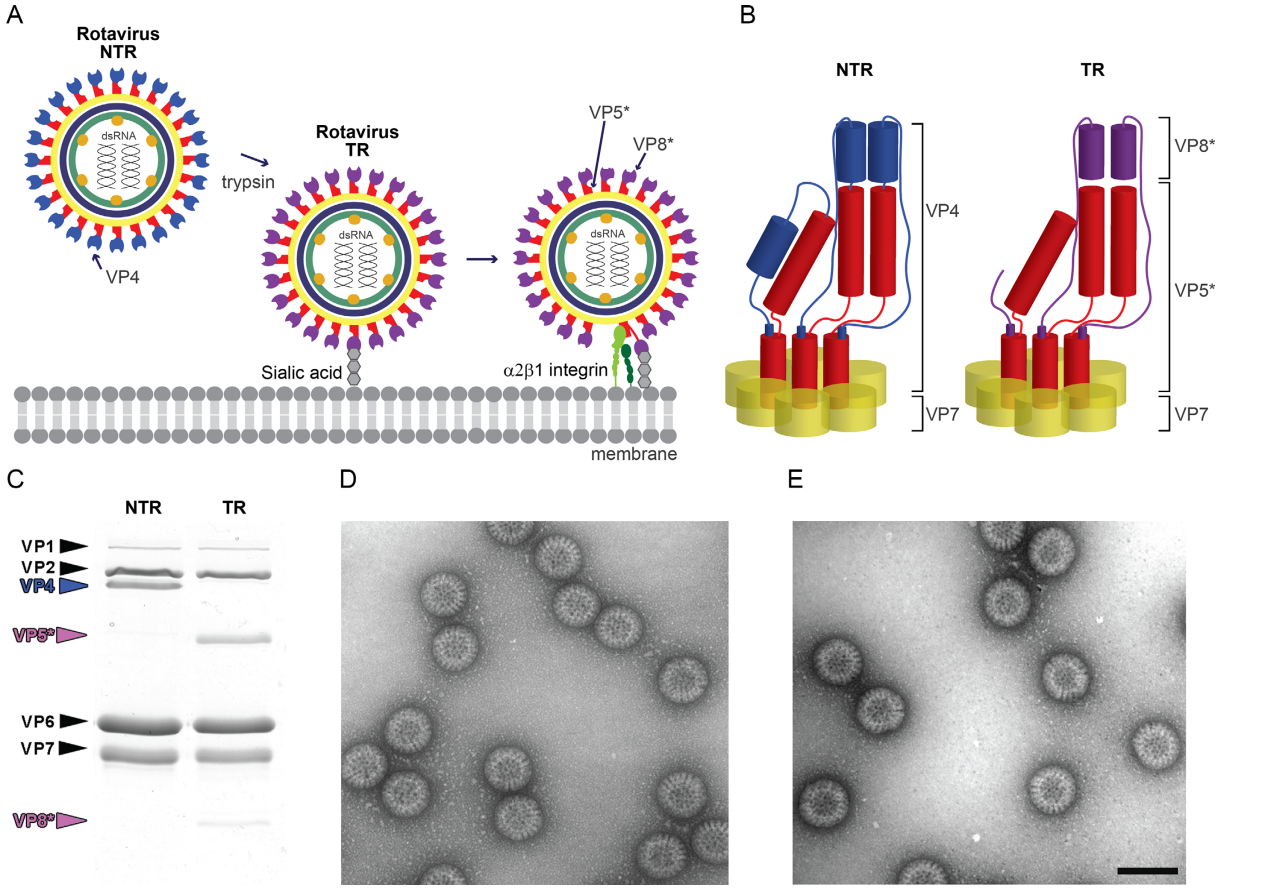

Figure 1. Probing rotavirus binding on cell surfaces and probing its binding to receptors. A) Schematic of rotavirus binding to the cell surface through sialic acid and $\alpha_2\beta_1$ integrin. TR are virions that are purified in the presence of trypsin. NTR are virions that are purified in the absence of trypsin. B) Schematic of outer capsid proteins before and after trypsinization. C) Coomassie blue-stained SDS–PAGE gels of purified SA11 NTR (left) and TR (right) (D,E) Transmission electron microscopy micrographs of negatively stained D) SA11 NTR- and E) TR-purified TLP (scale bar: 100 nm).

Rotaviruses' infectivity is also dependent on proteolytic enzymes. Treatment of the virions with trypsin results in the specific cleavage of VP4 into polypeptides denoted as VP8* and VP5*.[17,18] However, the protease cleavage does not result in loss of domains in at least two of the three subunits; due to the maintenance of their noncovalent bonds, the overall structures remaining similar after trypsinization,[19] indeed, and due to enhanced steric mobility, this process confers to the VP4 spikes the ability to fold back and promote membrane penetration[20] (Figure 1B), enhancing viral infectivity severalfold.[19] Further, the impact of cleavage on virus-binding properties to the various cell surface receptors remains unclear. To address this issue, here, we analyzed the molecular mechanism of sialidase-sensitive SA11 rotavirus strain binding to SA and $\alpha_2\beta_1$ integrin using force–distance (FD) curve-based atomic force microscopy (AFM). In doing so, we also developed a new robust algorithm to facilitate high-throughput retrieval of kinetics parameters that describe virus–receptor interactions. By comparing rotavirus binding properties to SA and $\alpha_2\beta_1$ integrin before and after treatment with trypsin, we conclude that trypsin treatment, while leading to increasing infectivity, does not affect receptor binding. We expanded on these observations and demonstrate that the engagement of integrin is dependent on their conformation and functional state, known to be regulated by divalent cations ($Mn^{2+} > Mg^{2+} > Ca^{2+}$).[21–24] Finally, we analyzed the dynamics of α_2 integrin subunit recruitment upon rotavirus binding to cell surfaces and demonstrated that an α_2 integrin-based peptide inhibits both the integrin binding identified and early cellular internalization processes required for virus uptake.

2. Results

2.1. VP8* Attaches to SA Glycans through Multivalent Bonds

As VP8* binding to SA glycans serves as the first foothold to cell surfaces upon virions landing, we wanted to probe the interaction forces established during these early binding events using FD-based AFM. To mimic cell surface glycans in vitro, streptavidin-coated surfaces were incubated with biotinylated SA (Figure S1, Supporting Information), and purified SA11 rotavirus (Figure 1C–E) were covalently attached at the AFM tip apex using a ≈15 nm-long polyethylene glycol (PEG) spacer (**Figure 2**A).[25] Validation of the purified SA11 rotavirus triple-layer virus particles (TLP) grown in the presence (trypsinized

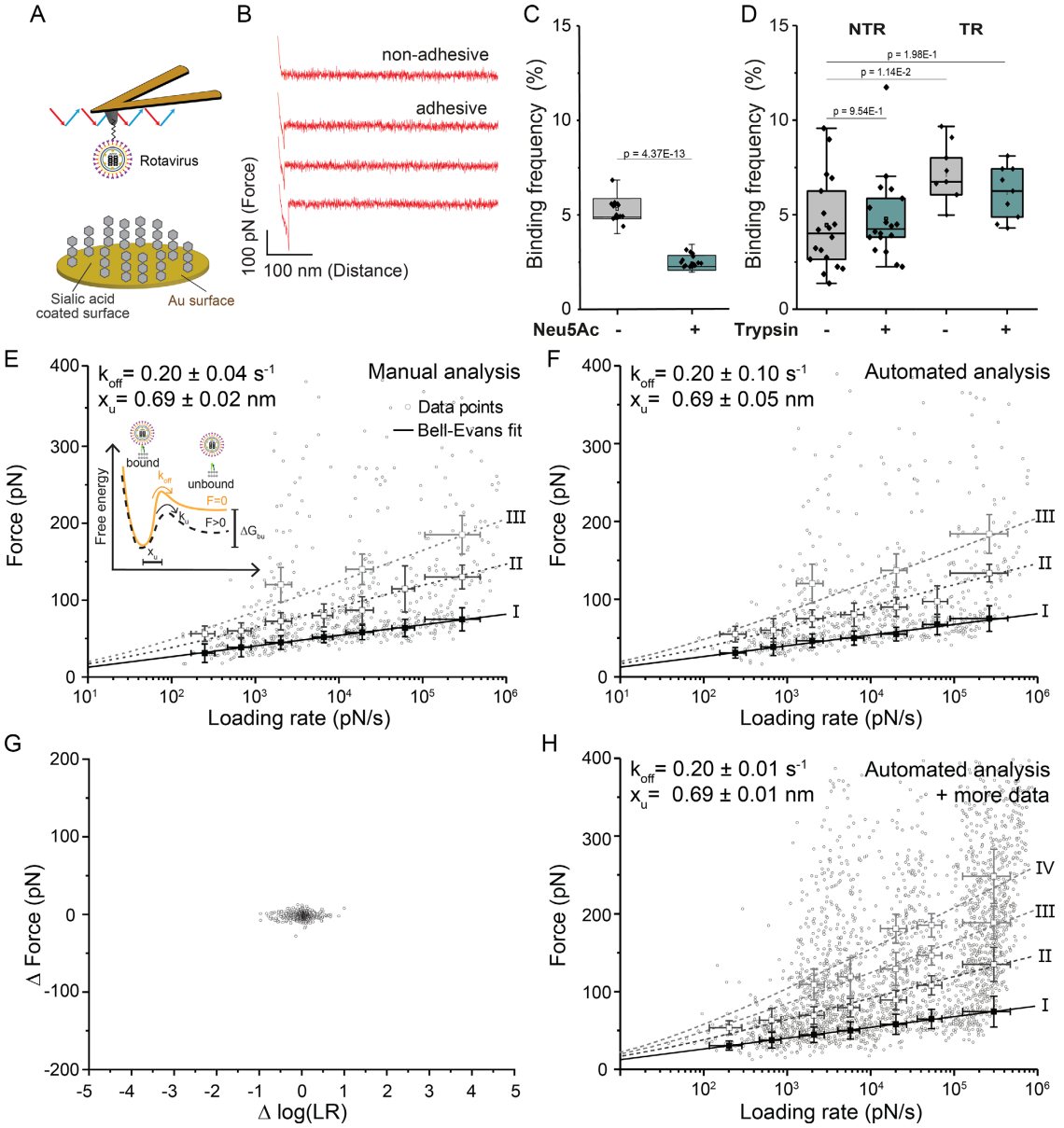

Figure 2. Probing rotavirus binding to sialic acid on model surface. A) Binding of single virion probed on a SA-coated surface. B) Representative FD curves (retraction part) showing either no binding event (nonadhesive) or specific binding events (adhesive curves). C) Box plot of specific BFs measured between SA11 TR and SA measured by AFM before and after injection of 1 mM Neu5Ac. D) Box plot of specific BFs measured between either SA11 NTR or TR and SA measured by AFM before and after incubation of rotavirus in trypsin TPCK (100 BAEE ml^{-1}, 37 °C, 30 min). Each data point represents the BF of 1024 individual measurements recorded at a retraction speed of 10 µm s^{-1}. The line in the box indicates median, the empty small square in the box indicates mean, the colored box indicates the 25th and 75th percentile, and the whiskers indicate the highest and the lowest values of the results. *P*-values were determined by two-sample *t*-tests in Origin. E,F) DFS plot showing the rupture force and as a function of the LR for interactions between SA11 TR and SA either extracted manually (E) or using the automated algorithm (F). The solid line shows the Bell–Evans fit of the single interaction and the dashed line the Williams–Evans prediction of the multivalent interactions. The error bar indicates standard deviation of the mean value. 627 curves recorded from two independent tips and samples. G) Difference of the values between manually analyzed and automatically analyzed in the force and the LR. H) Larger data set analyzed by the automated algorithm with the Bell–Evans fit and Williams–Evans prediction. 2364 curves recorded from six independent tips and samples.

virions [TR]) or absence (nontrypsinized virions [NTR]) of trypsin was conducted using PAGE gel (Figure 1C) and transmission electron microscopy (Figure 1D,E) before and after trypsin treatment. By approaching and retracting the AFM tip from the surface in a cyclic manner, FD curves were recorded (Figure 2B). Specific adhesion events were observed on ≈4–7% of retraction FD curves at rupture distances >5 nm, compatible with the extension of the PEG linker (Figure 2C).

After injection of free SA, a significantly lower binding frequency (BF) (<2%) is observed, confirming the specificity of the interaction. Next, we evaluated the influence of VP4 on the binding to SA after cleavage by trypsin. We compared TR- or NTR-purified virions (Figure 1C,D), as well as the influence of trypsin treatment of virions already immobilized on AFM tips. No significant differences were observed, though TR virions have a slightly higher binding probability to SA (≈6−7%) in comparison with NTR virions (≈4−5%). Taken together with cryogenic electron microscopy (cryo-EM) data, AFM results demonstrated that NTR and TR particles share the same fold overall structure, that is, in which at least two apical VP8* polypeptides remain linked to the virions even after cleavage of VP4 by the trypsin. This overall structure is SA-attachment competent for both TR and NTR (Figure 2D).[19]

To better characterize the binding properties of TR virions to SA, we extracted the kinetic parameters describing the VP8* interaction with SA. To this end, binding events were recorded by the FD curve-based AFM at various tip retraction speeds, enabling to explore the binding force over a wide range of loading rates (LRs) (Figure 2E). For each individual force–time (FT) curve (Figure 2B), the binding force, that is, the magnitude of the force just before the bond ruptures, and the LR, that is, the slope of the curve before the rupture, were extracted and displayed in a so-called dynamic force spectroscopy (DFS) plot (Figure 2E).[26] This analysis step is time-consuming and subject to variations from one person to another, depending on 1) the precision and 2) the selection of the regions of interest (ROIs), notably, for the extraction. Initially, we manually analyzed ≈600 FT curves for assessment (Figure 2E). Similar to other glycan-virus complexes studied by AFM, we observed binding forces in the range of 25−400 pN (Figure 2E; circles).[27–29] These wide range of forces depend on the pulling speed and originate from individual bonds or multiple bonds rupturing simultaneously. To confirm this, an analysis of force distribution was conducted for narrower LR ranges (Figure S4A, Supporting Information) and the means of the various peaks were plotted in the DFS graph (Figure 2E; squares). The kinetic parameters describing the single bond were then evaluated using the Bell–Evans model,[30,31] which describes the unbinding process as a simple two-state model, in which the bound state is separated from the unbound state by a single barrier located at a distance $x_u = 0.69 \pm 0.02$ nm and crossed with a transition rate of $k_{off} = 0.20 \pm 0.04\ s^{-1}$. The William–Evans[32] predictive model further confirmed the fast formation of multiple uncorrelated bonds loaded in parallel (Figure 2E, dashed lines). The entire analysis process encompassing the recording of the data through extraction of the kinetic parameters is long and fastidious (around 36−48 h per DFS plot). Due to the nature of the automated technique, the number of analyzed curves is important to reduce the error in the biophysical properties extracted via the Bell–Evans model, as more curves improve the clarity of peaks in the force histograms (Figure S4, Supporting Information). In other words, more analyzed curves help us distinguish multivalent bindings on the DFS plot easily and more correctly. Within this technique the robustness of the fit and the precision of the parameters strongly depend on the number of FD curves analyzed, comparable with trained manual analysis, but can be obtained far more rapidly.

2.2. Toward an Automated Analysis

To facilitate the analysis of extensive amounts of data, an algorithm has been developed to select the adhesive curves and automatically extract the binding forces and LRs (**Figure 3**). The algorithm mimics the manual process step by step (Figure 3A,B), although the order of the steps differs. A more detailed explanation about the algorithm workflow is provided in Supporting Information. Briefly, a baseline correction of the FT curve is applied, consisting of a force offset and a correction of the dragging force (Figure 3C,E).[33] Next, a validity check is conducted to sort adhesives curves from nonadhesives curves or curves showing nonspecific events (Figure 3D). This step of selecting the adhesive curves is based on both the height of the adhesion peaks and their positions within the force curve. Finally, the ROI encompassing the adhesive event is analyzed to extract the magnitude of the rupture force and the LR, corresponding to the slope of the curve just before the rupture event (Figure 3F). We applied the algorithm to the same data set previously analyzed manually (Figure 2F), revealing no significant difference (Figure 2H). Remarkably, the parameters extracted by the Bell–Evans model are equivalent. However, the algorithm is much faster (around 3−4 h per DFS plot) and enables the analysis of much larger data sets (Figure 2G), providing improved accuracy for the extracted parameters.

2.3. Rotavirus Specifically Binds to $\alpha_2\beta_1$ Integrins

After having shown that rotavirus establishes multiple bonds with SA moieties, we sought to study how rotavirus can specifically bind to $\alpha_2\beta_1$ integrins.[17] FD curve-based AFM was used to evaluate the interactions between the rotavirus grafted on the AFM tips and $\alpha_2\beta_1$ integrin covalently immobilized onto gold surfaces. $\alpha_2\beta_1$ integrin surfaces were validated by the scratching experiment, revealing a deposited layer of $\approx 3.7 \pm 1.0$ nm (Figure S5, Supporting Information). AFM experiments showed a BF of ≈8−10% (**Figure 4**A). To confirm that these binding events are specific, we conducted various control experiments (Figure 4A): 1) using an AFM tip without rotavirus (PEG linker terminated) or 2) a model surface without integrin. As anticipated, the BF was significantly lower confirming specificity (Figure 4A). As $\alpha_2\beta_1$ integrins bind to DGE sequences,[13] we also injected DGEA peptides, as another control, resulting in a similar reduction in the BF (Figure 4B). Together, these results confirm that rotavirus specifically binds to $\alpha_2\beta_1$ integrins under the experimental conditions described. Finally, we evaluated the influence of trypsinization (Figure 4C) and observed no influence, revealing that access to the binding epitope on the rotavirus is not modified by trypsin exposure.

2.4. An α_2 Subunit Integrin-Derived Peptide Inhibits Rotavirus Binding

Point mutations in α6 and αF regions of the α_2 subunit of the integrin significantly reduce rotavirus binding to CHO cells.[34] Based on this, we hypothesized that the regions of α_2 integrin may function as a rotavirus binding domain. We synthesized and evaluated a short peptide based on the α_2 subunit sequence

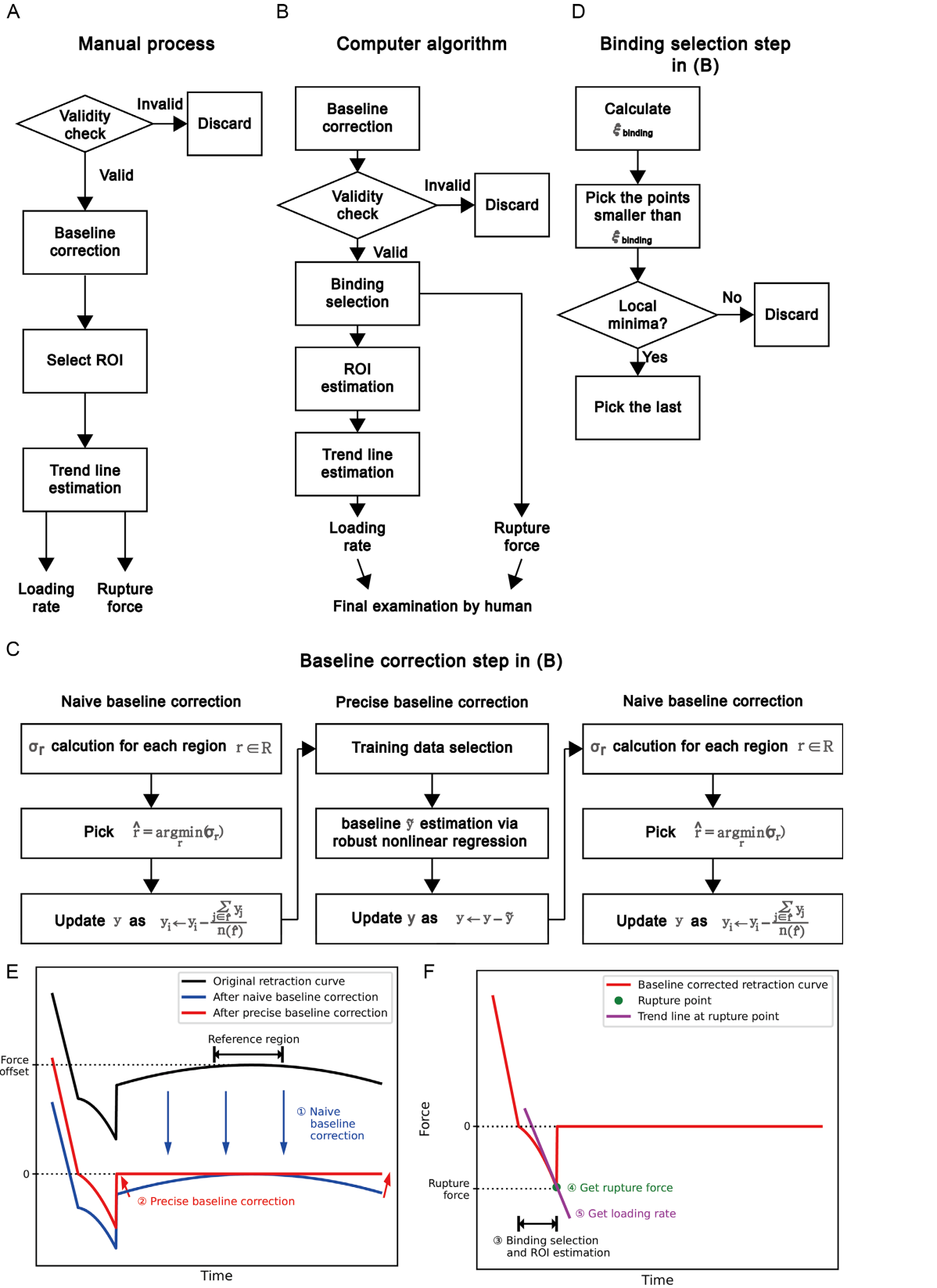

Figure 3. Toward automative data analysis. A) Overview of the principle of manual analysis of FD curves obtained by AFM. B–D) Automated procedure to analyze AFM FD curve with baseline correction step (C) and selection of specific binding events (D). E) Schematic of baseline correction step. F) Schematic of extracting the rupture force and the LR.

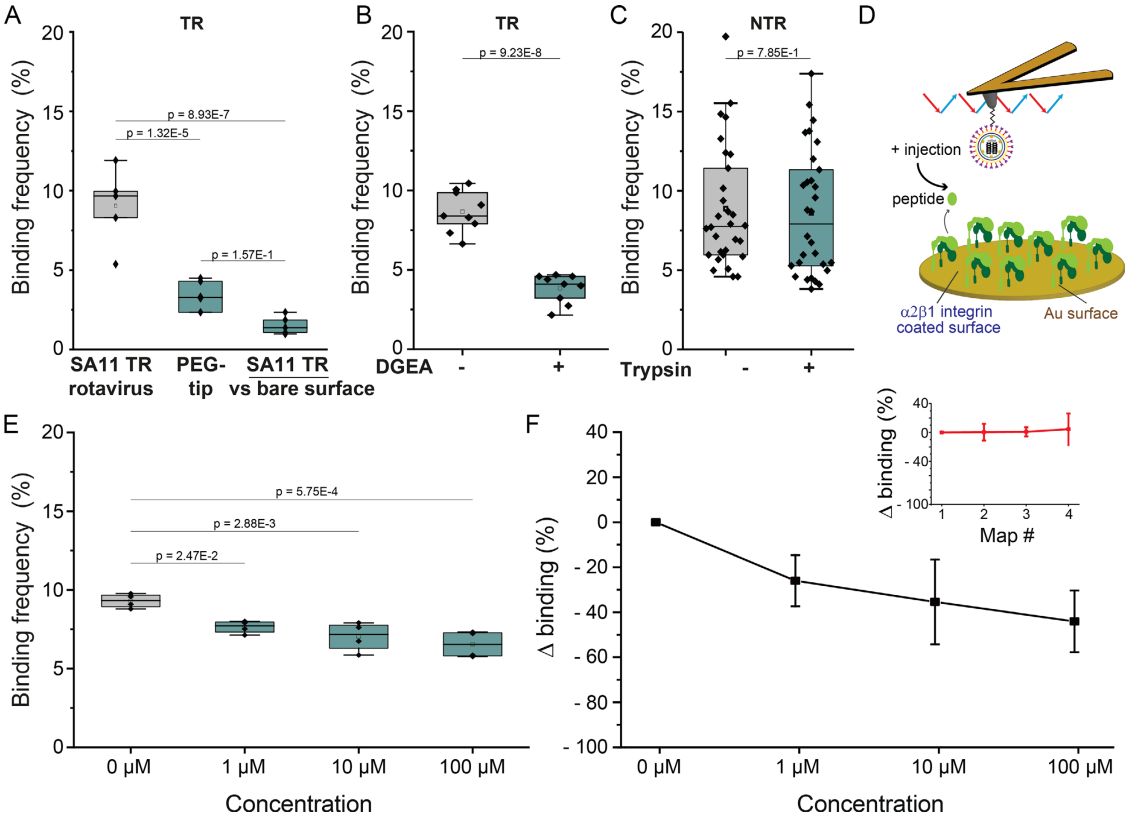

Figure 4. Probing rotavirus binding to $\alpha_2\beta_1$ integrin and evaluation of antibinding peptide properties. A) Box plot showing the specific BFs between the functionalized tips (SA11 TR or PEG) and the integrin-coated surface. B) Box plot showing the specific BF between SA11 TR and $\alpha_2\beta_1$ integrin before and after DGEA incubation (1 mM). C) Box plot showing the specific BF between SA11 NTR and $\alpha_2\beta_1$ integrin before and after incubation in trypsin (100 BAEE ml^{-1}, 37 °C, 30 min). D) Schematic of probing rotavirus binding to $\alpha_2\beta_1$ integrin in the presence of the peptide. E) Box plot showing specific probabilities between rotavirus SA11 TR and $\alpha_2\beta_1$ integrin in the presence of the peptide at various concentrations (1 μM, 10 μM, 100 μM). Each data point corresponds to the BF extracted from one map recorded at a 10 μm s^{-1} retraction speed. The line in the box indicates median, the empty small square in the box indicates mean, the colored box indicates the 25th and 75th percentile, and the whiskers indicate the highest and the lowest values of the results. F) Graph showing the difference of BF after peptide injection. The error bar indicates standard deviation of the mean value. The inset refers to the control with the virus buffer injection, showing that the consecutive mappings do not influence the BP. *P*-values were determined by two-sample *t*-test in Origin.

([320-338]: DTKNLIKEIKAIASIPTE), examining its utility in preventing virus binding to $\alpha_2\beta_1$ integrins. Using our single-molecule approach, we tested various peptide concentrations in the range of 1−100 μM (Figure 4D) and observed progressive concentration-dependent reduction in the rotavirus BF to the integrins (Figure 4E). The α_2-derived peptide led to a 44 ± 14% reduction of the BF at 100 μM (Figure 4F), whereas repetitive mappings in absence of the peptide did not influence the BF (Figure 4F, inset). This experiment confirms the role of the α_2 subunit in the interaction with rotaviruses but also demonstrates that a short peptide based on the α_2 sequence is a promising approach to block rotavirus binding to cell surface integrins, identified as key receptors mediating cell entry. This α_2-derived peptide merits further study as a potential therapeutic option.

2.5. Cation Dependency on $\alpha_2\beta_1$ Integrin–Rotavirus Binding

Conformation and affinity of $\alpha_2\beta_1$ integrins for their ligand are known to be modulated by divalent cations (Ca^{2+}, Mg^{2+}, Mn^{2+}) (**Figure 5**A).[21–24] To evaluate the influence of the various cations on $\alpha_2\beta_1$ integrins binding, we first compared the BFs (Figure 5B) and observed that the BF drops in the order Mn^{2+}>Mg^{2+}>Ca^{2+}, which is in good agreement with the anticipated affinity states. These results suggest that that binding to integrin is regulated by various divalent cations and highlight the physiological relevance of the results reported here. Based on these data, we further investigated the kinetics properties of the binding for each cation (Figure 5C–H). Using the FD curve-based AFM at different LRs, we analyzed the rupture forces and plotted the force–LR dependency for Ca^{2+} (Figure 5D), Mg^{2+} (Figure 5F), and Mn^{2+} (Figure 5H). Next, we analyzed the distribution of these forces for more narrow LR ranges (Figure S6, Supporting Information) and the means of the various peaks were plotted in each DFS graph (Figure 5D,F,H; squares). The dissociation rate (k_{off}) and distance to the transition state (x_u) of the binding free-energy landscape were extracted using the Bell–Evans model. While the extracted x_u is similar for the three cations, suggesting a similar binding pocket, their various k_{off} are

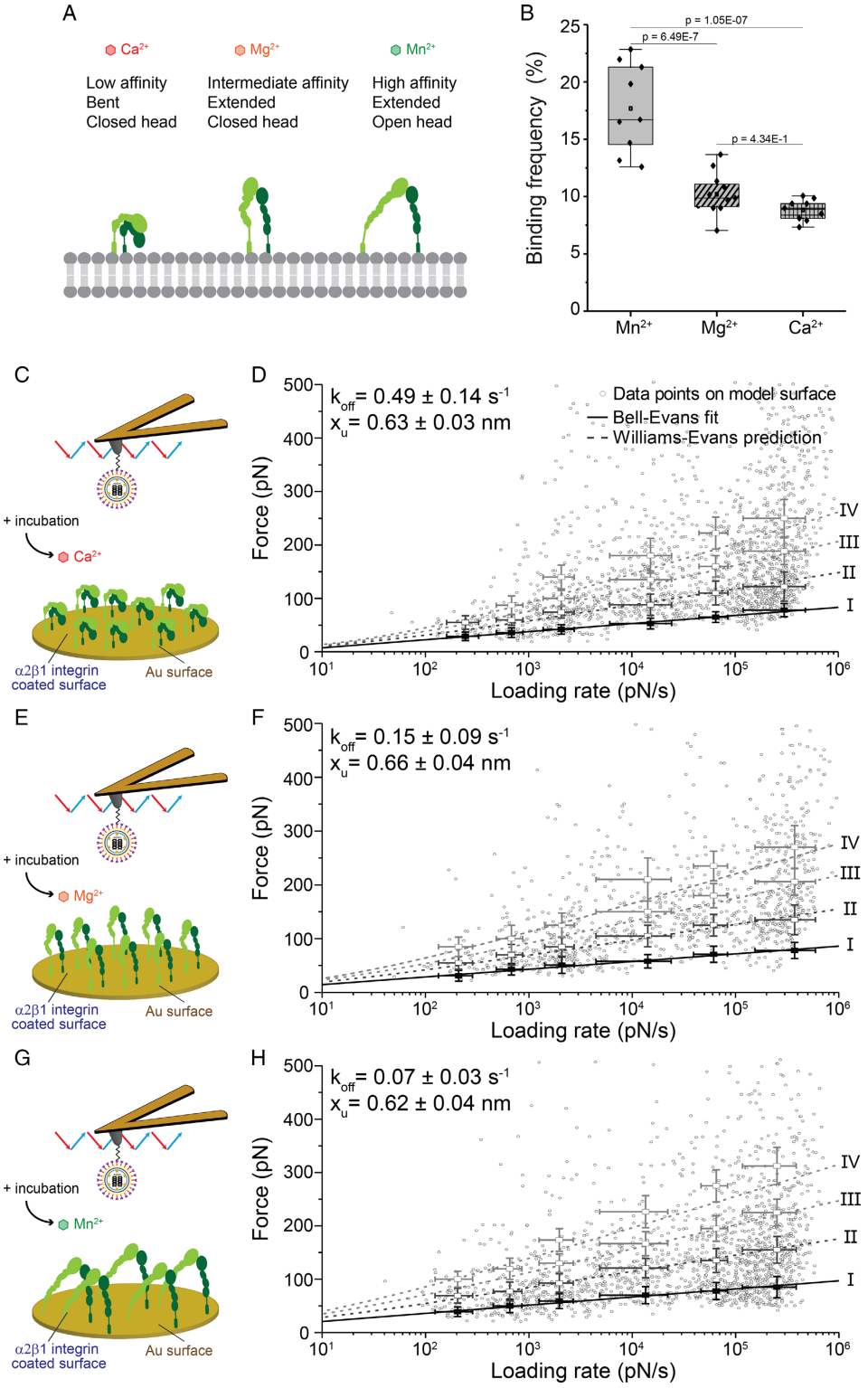

Figure 5. Probing the effect of the conformation of $\alpha_2\beta_1$ integrin by divalent cation on the binding of rotavirus on the model surface. A) Schematic of $\alpha_2\beta_1$ integrin cation-dependent conformations in presence of either Ca^{2+}, Mg^{2+}, or Mn^{2+}. B) Box plot showing specific BF between rotavirus SA11 TR and $\alpha_2\beta_1$ integrin in the presence of either Ca^{2+}, Mg^{2+}, or Mn^{2+}. One data point corresponds to the BF extracted from one map. The line in the box indicates median, the small square in the box indicates mean, the colored box indicates the 25th and 75th percentile, and the whiskers indicate the highest and the lowest values of the results. *P*-values were determined by two-sample *t*-test in Origin. (C–H) Schematic of probing rotavirus SA11 TR binding to integrin $\alpha_2\beta_1$ in the presence of Ca^{2+} (C,D, 1794 curves), Mg^{2+} (E,F, 1145 curves), and Mn^{2+} (G,H, 1729 curves) using AFM and respective DFS plots (D,F,H). Experiments were reproduced at least four times with independent tips and samples.

Table 1. Comparison of thermodynamic parameters for rotavirus binding to $\alpha_2\beta_1$ integrins in the presence of Mn^{2+}, Mg^{2+}, or Ca^{2+}.

	BP [%]	k_{off} [s^{-1}]	x_u [nm]
Mn^{2+}	17.69 ± 1.97	0.07 ± 0.03	0.62 ± 0.04
Mg^{2+}	10.20 ± 0.88	0.15 ± 0.09	0.66 ± 0.04
Ca^{2+}	8.83 ± 0.47	0.49 ± 0.14	0.63 ± 0.03

different. The measurement made in the presence of Ca^{2+} shows the highest k_{off} ($0.49 \pm 0.14\ s^{-1}$) (Figure 5C,D), whereas Mg^{2+} and Mn^{2+} show lower k_{off}, $0.15 \pm 0.09\ s^{-1}$ and $0.07 \pm 0.03\ s^{-1}$, respectively (Figure 5F,H). These results indicate that the rotavirus–integrin bond is stabilized by Mn^{2+} and Mg^{2+} and is less stable in the presence of Ca^{2+} (**Table 1**).

2.6. Rotavirus Binding Promotes α_2 Integrin Recruitment

After having shown rotavirus binding properties to $\alpha_2\beta_1$ integrins on model surfaces (Figure 4, 5), we wanted to explore the physiological relevance directly on living cells. To this end, we grafted the rotavirus on a fluorescently labeled gold nanoparticle (NP). A single NP was captured at the end of a fluidic force microscopy (FluidFM) tip using negative pressure.[21,35] The NP was then brought into contact with the cell surface by applying a force of 300 pN and was held in place. By keeping the virion-laden NP in direct physical contact with the cell membrane in a static manner, we were able to monitor the dynamics of fluorescently labeled α_2-integrin-subunit recruitment, as previously shown for the other virus-receptor interactions (**Figure 6**A).[21] Using this approach with transfected CHO cells, we observed the recruitment of α_2 integrin around the NP (Figure 6B,D, and Movie S1, Supporting Information), confirming that the interaction is also established in the cellular context. As a control, we tested a nonfunctionalized NP and did not observe any recruitment (Figure 6C,D, Figure S7, and Movie S2, Supporting Information). Next, we tested our α_2-derived peptide and showed that after peptide treatment, the recruitment of α_2-integrin is completely abolished (Figure 6C,D, Figure S7, and Movie S3, Supporting Information). These data suggested that recruitment of α_2 integrin is induced after rotavirus binding to α_2 integrin specifically. Taken together, we demonstrated that rotavirus interacts with integrins in a cellular context and that these interactions can be inhibited by a short peptide based on α_2-integrin-subunit sequence.

3. Discussion

The technique of FD-based AFM is poised to become a valuable tool for the quantitative and dynamic characterization of virus binding to cell surface receptors as several studies of single-virus binding to the receptor have been done with FD-based AFM.[21,27,36] However, to facilitate high-throughput demand, there was an unmet need to develop a methodology allowing rapid screening, for example, viral antiadhesive molecules on living cells.

To address this issue, here, we developed an automated tool allowing fast extraction and analysis of the curves recorded by FD-based AFM to characterize the biophysical properties uncovering how virus entry into cells is regulated. The automated tool dramatically reduces the time needed to sort FD curves, as well as extract LRs and rupture forces from these large data sets. This permits quantifying the dynamics of virus binding to the cell surface significantly faster. Moreover, its performance showed good accuracy on par with human analysis. It is hoped that this tool could be used to obtain more reproducible and accurate values for k_{off}, x_u, and BF, through standardization and removal of human error or subjectivity. Therefore, this tool will be the first step to make the analysis procedure automatical. The approach described demonstrates the utility of AFM as an effective platform for rapid screening of antibinding candidates.

Using the algorithm, we investigated whether protease treatment (specifically trypsin) influences rotavirus binding potential to cell surface glycans (SA) and entry receptors ($\alpha_2\beta_1$ integrins). Although the VP4 spike protein is cleaved into VP8* and VP5* fragments by trypsin,[20] VP8* fragments remain linked to VP5* after trypsinization, and evidence suggests that infectivity is enhanced,[22] leading to the hypothesis that binding potential to either SA or $\alpha_2\beta_1$ integrins could be influenced by the cleavage. However, our experiments conducted at the single-virus level did not reveal any significant difference. The crystal structures of VP4 before and after trypsinization have previously been identified as similar.[19] Trypsinization may not induce conformational change. Therefore, trypsinization of rotavirus might not be a key requirement for rotavirus to infect cells; instead, after binding to sialic acids, this can induce the conformational changes of the spike protein. The conformational change may alter the biophysical properties of the binding with other receptors such as hsc70, $\alpha_V\beta_3$, $\alpha_x\beta_2$, and $\alpha_4\beta_1$.

Next, we investigated whether the binding to integrin is affected by its activation state, as the conformation of $\alpha_2\beta_1$ integrins is strongly influenced by the presence of divalent cations (Ca^{2+}, Mg^{2+}, or Mn^{2+}), which in turn modulate its affinity state for its cognate ligand. Our experiments reveal that binding established between $\alpha_2\beta_1$ integrins and rotavirus exhibits the same behavior. In particular, Mn^{2+} is known to promote the extended open headpiece conformation,[22–24] resulting in a 2−7 times longer lifetime of the integrin–rotavirus complex. As DGE sequences, which are the binding motifs to $\alpha_2\beta_1$ integrins, locate in the root part of VP4 (PDB: 6WXE),[20] the extended $\alpha_2\beta_1$ integrins approach easily and bind to VP4 protein more stably. Both active and inactive integrins are endocytosed from the plasma membrane,[37] so the binding property of integrins to ligands is a critical factor for endocytosis of molecules, especially in virus infection.[38] This phenomenon will be interesting in viral tropism research.

Using our FluidFM experiments, we demonstrated that rotavirus at the cell surface actively promotes the recruitment of integrins. Rotavirus binding to α_2 integrins is critical for inducing this recruitment. The following studies are needed further on the activation of intracellular signaling after rotavirus binding-induced integrin recruitment. It will help us understand the rotavirus infection mechanism.

The recruitment of α_2 integrins was almost totally inhibited when the inhibitory peptide was administered, while observing the behavior of α_2 integrin. A protein-derived peptide, taken from

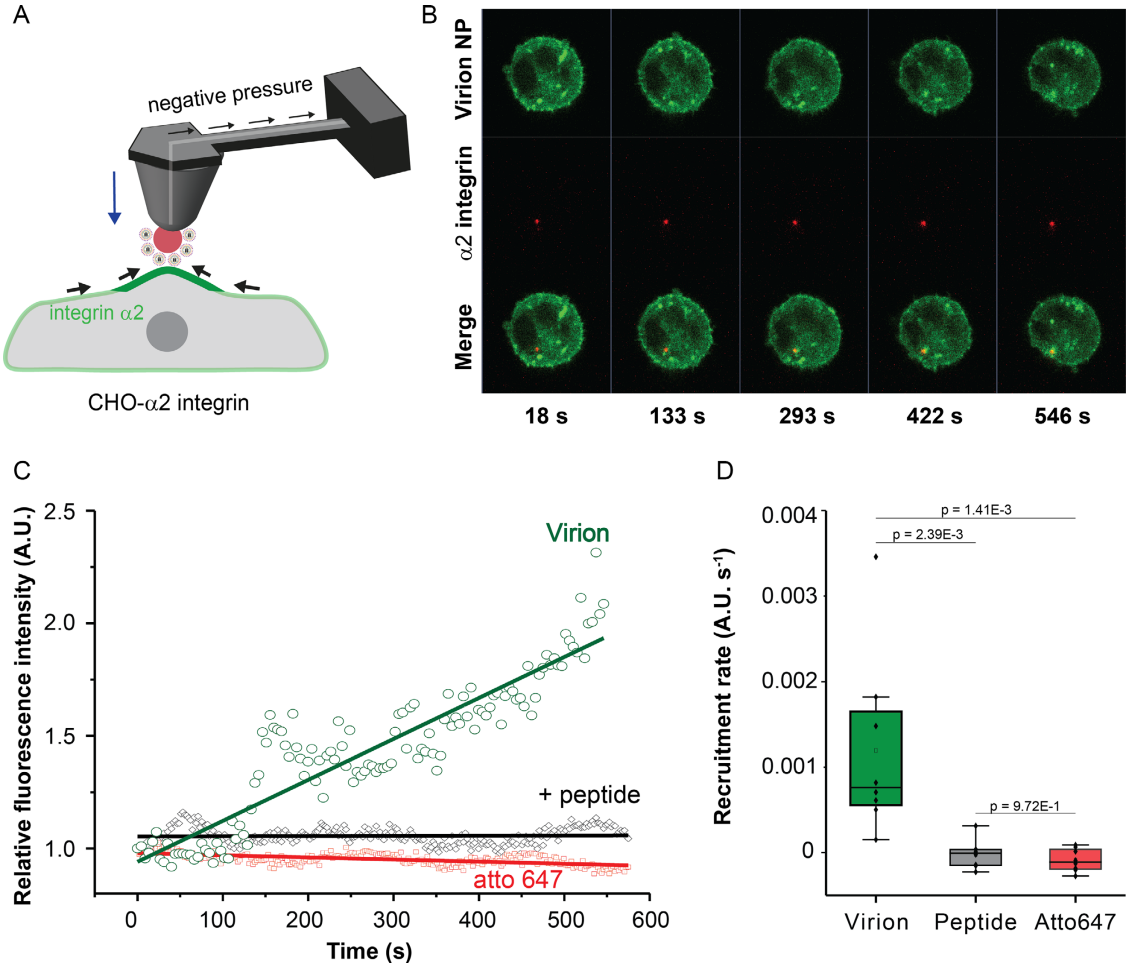

Figure 6. α_2 integrin recruitment to SA11 rotaviruses upon cell surface contact. A) Schematic of probing rotavirus binding to cell surfaces using FluidFM. A NP coated with fluorescently labeled rotavirus is trapped at the end of the microchanneled cantilever and put into contact with a CHO cell that expresses mCherry-α_2 integrin (represented in green for better visibility). B) Representative time-series images showing α_2 integrin recruitment toward the NP coated with rotavirus SA11 TR virions. C) Graph showing the normalized fluorescence signal extracted from the region around the NP (red in B). D) Box plot showing the α_2 integrin recruitment rate. The rate was extracted from the slope of the linear fit conducted on (C). The line in the box indicates median, the small square in the box indicates mean, the colored box indicates the 25th and 75th percentile, and the whiskers indicate the highest and the lowest values of the results. All data are representative of at least $N = 8$ independent experiments. Each data point corresponds to the recruitment rate extracted from one cell recorded for 10 min. *P*-values were determined by the two-sample *t*-test in Origin.

the binding region, is an accepted way to inhibit the interaction between proteins. Arg-Gly-Asp (RGD)/Lys-gly-glu (KGE) peptides block the interaction between integrins and their ligands. A tyrosine kinase blocking collagen IV-derived peptide blocks the interaction between VEGF and its receptor.[39] HLA-derived peptides block cytotoxicity by binding to β-Tubulin[40] and A SDF-1-derived peptide to inhibit the interaction between HIV-1 and its receptor CXCR4.[41] Moreover, to inhibit the infection of SARS-CoV-2, many kinds of ACE2 receptor-derived peptides were tested, and they successfully inhibited its binding on the ACE2 receptor and its infection.[25,42,43] Protein-derived peptides are designed rationally and their effect is promising. Utilizing protein-derived peptides would be important in therapeutics in the near future.

4. Conclusion

Based on our biophysical analysis and the observation that a point mutation in the α2 integrin subunit leads to a significant reduction in rotavirus infectivity,[32] we synthesized an 18 amino acid-long peptide that shows promising antibinding properties between the rotavirus and immobilized integrins. More interestingly, this antibinding peptide appears to be even more potent in a cellular context, where it completely abolishes the recruitment of integrins after virion cell surface attachment. The experimental approach framed here offers a new perspective for treating rotavirus infection and more broadly for investigating the binding of viruses to their target receptors either in isolation or in a cellular context.

5. Experimental Section

Generation of Rotavirus Stocks: The clone C4111 of simian agent 11 rotavirus strain (SA11) was used within three passages of the last plaque isolation step.[19] The virus was amplified using the monkey epithelial cell line MA104 (ECACC 85 102 918) cultured in MEM with 10% fetal calf serum and used between passages 10 and 24. A detailed description of the experimental procedures used for the preparation of highly purified viral particles has been previously published.[19] Briefly, for the preparation of TLP in the presence of trypsin (TR), infections were carried out in MEM containing 10 BAEE U ml^{-1} TPCK-trypsin. For the preparation of rotavirus TLP with intact VP4 (NTR), cell monolayers were washed three times with MEM after virus adsorption and MEM containing 0.5 μg of the protease inhibitor leupeptin. Supernatants from infected cells were clarified by centrifugation, concentrated using PEG-8000, and purified by double-band isolation in CsCl gradients. The structural integrity of the final preparations was verified by transmission electron microscopy after negative staining.

Cell Culture and Transfection: CHO cells were cultured in Ham's F-12 Nutrient Mix (10 % fetal bovine serum, penicillin [100 U mL^{-1}], and streptomycin [100 μg mL^{-1}]) at 37 °C in a humidified atmosphere (5% CO_2). We transfected cells with mCherry-Integrin-Alpha2-N-18 plasmid (#55 063, Addgene) using Lipofectamine LTX (Invitrogen).

Functionalization of AFM Cantilevers: MSCT-D cantilevers (Bruker) were functionalized with rotavirus SA11 to conduct FD-based AFM on model surfaces. NHS-PEG24-Ph-aldehyde linkers were linked between rotavirus and the tip, as previously described.[25] In brief, the cantilevers were washed in chloroform for 10 min, cleaned in a UV radiation and ozone (UV–O) cleaner (Jet light), immersed in ethanolamine solution (3.3 g in 6.6 mL of DMSO) overnight, and immersed in DMSO and ethanol three times. The cantilevers were immersed in the NHS-PEG24-Ph-aldehyde solution (3.3 mg in 500 μL of chloroform and 30 μL of triethylamine) after washing and washed with chloroform three times, dried with nitrogen, and then immersed in 50 μL of virus solution (≈10^8–10^9 virions mL^{-1}) with 2 μL of $NaCNBH_3$ solution (6% in 0.1 M NaOH) for 1 h on ice to be functionalized with rotavirus. 5 μL of 1 M ethanolamine solution was added to the solution to quench the reaction and they were washed in the virus buffer three times.[44]

Preparation of SA-Coated Model Surfaces: Biotinylated bovine serum albumin (25 μg mL^{-1}) was incubated on freshly cleaned (UV–ozone) gold-coated silicon surfaces at 4 °C overnight. After subsequent washing with PBS, streptavidin (10 μg mL^{-1}) was added, surfaces incubated for 2 h, followed by washing with PBS and incubation of biotinylated 3'-sialyl-*N*-acetyllactosamine (10 μg mL^{-1}, Dextra) for 2 h. The resulting surfaces were washed with PBS.

Rotavirus Trypsinization: A rotavirus-grafted cantilever was incubated with trypsin TPCK (100 BAEE ml^{-1}, #11 896 734, Pierce) at 37 °C for 30 min and then washed three times in virus buffer. The trypsinized rotavirus-grafted tip was used immediately to measure the BF.

α2β1 Integrins-Coated Model Surfaces: $\alpha_2\beta_1$ integrin protein (R&D systems, 5698-A2-050) was immobilized on gold-coated surfaces using NHS–EDC chemistry. Gold-coated surfaces were washed with ethanol and dried with nitrogen and cleaned in a UV radiation and ozone (UV–O) cleaner (Jet light). The surfaces were incubated in alkanethiol solution (99% 1 mM of 11-mercapto-1undecanol and 1% 1 mM 16-mercaptohexadecanoic acid) overnight and rinsed with ethanol and dried with nitrogen and immersed in the NHS–EDC solution (40 mg of *N*-hydroxysuccinimide [NHS] and 100 mg of 1-ethyl-3-(3-dimethylaminopropyl)carbodiimide [EDC] in 4 mL of Milli-Q water) for 30 min. They were rinsed with Milli-Q water and incubated in $\alpha_2\beta_1$ integrin solution (0.1 μg μL^{-1}) and then washed in PBS.

FD-Based AFM on Model Surfaces: Functionalized MSCT-D probes (Bruker) were used for FD-based AFM on model surfaces. The spring constant of probes was calculated by a thermal tune.[45] The experiments were conducted in the virus buffer at room temperature. The force volume (contact) mode of AFM Nanoscope Multimode 8 (Bruker) was used to conduct FD-based AFM (Nanoscope software v9.1). It scanned the areas (5 × 5 μm) with 32 × 32 pixels of resolution, 1 Hz of line frequency, 500 nm of ramp size set, and 500 pN of setpoint force.

DFS Analysis: For analysis of DFS experiments, LR and rupture forces were extracted from the curves, which were recorded with variable retraction speeds (0.1, 0.2, 1, 10, 20 μm s^{-1}) using the automated tool. To display the DFS plots and fit histograms of data distribution, Origin software (OriginLab) was used.

Peptide Blocking Assay: α_2-integrin subunit-derived peptide (LDTKNLIKEIKAIASIPTE, 320-338) was obtained from ChinaPeptides. To verify the impact of the peptide, the binding probability was measured before injecting and after injecting, 1 μM, 10 μM, and 100 μM of the peptide. The data were recorded with 1 μm s^{-1} approach and 10 μm s^{-1} retraction speed on the Nanoscope Multimode 8 (Bruker).

Functionalization of Gold NPs with Rotavirus Particles: Gold NPs of 400 nm diameter (Sigma) were functionalized with rotavirus SA11 virions through standard NHS–EDC coupling chemistry. 500 μL of NP suspension (nominal concentration: 10^8 NP mL^{-1}) was centrifuged for 10 min at 20 000 g. The supernatant was removed and the NPs were resuspended in 200 μL of solution (500 μL of 1 mM 11-mercapto-1-undecanol solution (Sigma), 160 μL of 1 mM 16-mercaptohexadecanoic acid (Sigma), 16 μL of 1 mM 11-Amino-1-undecanethiol hydrochloride, and 104 μL of ethanol and incubated overnight at room temperature on a shaker. The NPs were washed twice with 200 μL of ethanol by centrifugation. The NPs were resuspended and immersed in an NHS–EDC solution for 30 min on a shaker. The NPs were washed one time with 200 μL of the virus buffer by centrifugation and resuspended in the buffer and 10 μL of virus solution (≈10^{11}–10^{12} particles mL^{-1}) was added to the solution and incubated for 60 min on a shaker. 2 μL of Atto 647N NHS ester was added in the solution and incubated for 60 min more. They were centrifuged (10 min, 20 000 g) and resuspended in 200 μL of the virus buffer.

Functionalization of Gold NPs with Atto 647N Dye: The NPs were functionalized with an Atto 647N dye (Atto-Tec) for control experiments. 500 μL of NP suspension (nominal concentration: 10^8 NP mL^{-1}) was centrifuged for 10 min at 20 000 g. The supernatant was removed and the NPs were resuspended in 200 μL of cysteamine solution (100 mM) and incubated overnight on a shaker. The NPs were washed twice with 200 μL of ethanol by centrifugation. The NPs were resuspended in 200 μL of $NaHCO_3$ (pH: 8.5), and 1 μL of Atto 647 NHS ester (Atto-Tec, 10 mg mL^{-1}) was added to the solution and incubated for 30 min on a shaker in the dark. The NPs were centrifuged (10 min, 20 000 g) and resuspended in 200 μL of $NaHCO_3$.

α_2 Integrin Recruitment Dynamics: α_2 integrin recruitment was followed in real time by live-cell confocal microscopy (Zeiss, LSM980) using FluidFM (Cytosurge) coupled to a Bruker Resolve AFM. Petri dishes were coated with 2 mL of concanavalin-A solution (2 mg mL^{-1}) for 2 min and then aspirated and allowed to dry in a tissue-culture hood for 1 h. Transfected cells with mCherry-Integrin-Alpha2-N-18 plasmid (#55 063, Addgene) were seeded on the plate in 2 mM Mn^{2+}-supplemented media right before the experiment.

Virus-functionalized NPs were held in place by a FluidFM microchanneled cantilever[21] using negative pressure of 800 mbar. The cantilever was brought in contact with a cell using an applied force of 300 pN for 10 min. Time-series (XYT) images (100 × 100 nm) were recorded by confocal microscopy LSM-980 (Zeiss) equipped with Airyscan, a water-immersion lens (×63, NA 1.20, Zeiss C-Apochromat), GaAsP–PMT detectors, and helium–neon and argon lasers (561 and 639 nm). Confocal images were treated with Zen blue 3.3 software (Zeiss) and analyzed using Fiji (Time-series analyzer). A circular ROI was drawn using the NP and the average intensity of mCherry signal was retrieved. As photobleaching occurred during the observation window (10 min), another ROI of the same size was used to determine background signal decay. Photobleaching was compensated by dividing the intensity of the NP-derived area by that of the background area.

Statistical Analysis: The raw data obtained from AFM were treated by Nanoscope software v9.1 (Bruker) and the algorithm that the authors developed. Data were presented as the mean ± SD for Figure 2E,F, H,4F,5D,F,H. All other graphs showed that the line in the box indicated median, the small square in the box indicated mean, the colored box indicated the 25th and 75th percentile, and the whiskers indicated the highest and the lowest values of the results. *P*-values were determined by

two-sample *t*-test in Origin 2017. The exact *P*-value was represented in each graph. The sample size varied depending on the experiments. The size was specified in each figure legend.

Supporting Information

Supporting Information is available from the Wiley Online Library or from the author.

Acknowledgements

J.Y. and J.P. contributed equally to this work. This work was supported by the Université catholique de Louvain and the Fonds National de la Recherche Scientifique (F.R.S.-FNRS). This project received funding from the European Research Council under the European Union's Horizon 2020 research and innovation program (grant agreement no. 758224), from the FNRS-Welbio (grant no. CR-2019S-01), from the Spanish Ministry of Economy and Competitivity BFU2013-43149-R, and from the ISCIII AESI PI20CIII/00014. The funders had no role in study design, data collection and analysis, decision to publish, or preparation of the manuscript.

Conflict of Interest

The authors declare no conflict of interest.

Data Availability Statement

The data that support the findings of this study are available from the corresponding author upon reasonable request.

Keywords

antiviral, atomic force microscopy, automated analyzing tools, blocking, integrins, rotavirussingle-molecule

Received: June 23, 2021
Revised: July 27, 2021
Published online: August 11, 2021

[1] C. Troeger, I. A. Khalil, P. C. Rao, S. Cao, B. F. Blacker, T. Ahmed, G. Armah, J. E. Bines, T. G. Brewer, D. V. Colombara, G. Kang, B. D. Kirkpatrick, C. D. Kirkwood, J. M. Mwenda, U. D. Parashar, W. A. Petri, Jr., M. S. Riddle, A. D. Steele, R. L. Thompson, J. L. Walson, J. W. Sanders, A. H. Mokdad, C. J. L. Murray, S. I. Hay, R. C. Reiner, Jr., *JAMA Pediatr.* **2018**, *172*, 958.
[2] S. D. Trask, S. M. McDonald, J. T. Patton, *Nat. Rev. Microbiol.* **2012**, *10*, 165.
[3] J. Angel, M. A. Franco, H. B. Greenberg, *Nat. Rev. Microbiol.* **2007**, *5*, 529.
[4] S. Esposito, B. Camilloni, S. Bianchini, G. Ianiro, I. Polinori, E. Farinelli, M. Monini, N. Principi, *Virol. J.* **2019**, *16*, 64.
[5] F.-T. Wu, K. Bányai, B. Jiang, L. T.-C. Liu, S. Marton, Y.-C. Huang, L.-M. Huang, M.-H. Liao, C. A. Hsiung, *Sci. Rep.* **2017**, *7*, 40731.
[6] C. F. Arias, D. Silva-Ayala, S. López, *J. Virol.* **2015**, *89*, 890.
[7] L. Fiore, H. B. Greenberg, E. R. Mackow, *Virology* **1991**, *181*, 553.
[8] E. M. Fuentes-Pananá, S. López, M. Gorziglia, C. F. Arias, *J. Virol.* **1995**, *69*, 2629.
[9] P. R. Dormitzer, Z.-Y. J. Sun, G. Wagner, S. C. Harrison, *EMBO J.* **2002**, *21*, 885.
[10] S. Zárate, M. A. Cuadras, R. Espinosa, P. Romero, K. O. Juárez, M. Camacho-Nuez, C. F. Arias, S. López, *J. Virol.* **2003**, *77*, 7254.
[11] C. A. Guerrero, D. Bouyssounade, S. Zárate, P. Isa, T. López, R. Espinosa, P. Romero, E. Méndez, S. López, C. F. Arias, *J. Virol.* **2002**, *76*, 4096.
[12] M. Ciarlet, S. E. Crawford, E. Cheng, S. E. Blutt, D. A. Rice, J. M. Bergelson, M. K. Estes, *J. Virol.* **2002**, *76*, 1109.
[13] K. L. Graham, P. Halasz, Y. Tan, M. J. Hewish, Y. Takada, E. R. Mackow, M. K. Robinson, B. S. Coulson, *J. Virol.* **2003**, *77*, 9969.
[14] M. J. Hewish, Y. Takada, B. S. Coulson, *J. Virol.* **2000**, *74*, 228.
[15] B. S. Coulson, S. L. Londrigan, D. J. Lee, *Proc. Natl. Acad. Sci.* **1997**, *94*, 5389.
[16] L. Hu, S. E. Crawford, R. Czako, N. W. Cortes-Penfield, D. F. Smith, J. Le Pendu, M. K. Estes, B. V. Prasad, *Nature* **2012**, *485*, 256.
[17] S. López, C. F. Arias, *Trends Microbiol.* **2004**, *12*, 271.
[18] S. E. Crawford, S. K. Mukherjee, M. K. Estes, J. A. Lawton, A. L. Shaw, R. F. Ramig, B. V. Prasad, *J. Virol.* **2001**, *75*, 6052.
[19] J. M. Rodríguez, F. J. Chichón, E. Martín-Forero, F. González-Camacho, J. L. Carrascosa, J. R. Castón, D. Luque, *PLOS Pathog.* **2014**, *10*, 1004157.
[20] T. Herrmann, R. Torres, E. N. Salgado, C. Berciu, D. Stoddard, D. Nicastro, S. Jenni, S. C. Harrison, *Nature* **2021**, *590*, 666.
[21] M. Koehler, S. J. L. Petitjean, J. Yang, P. Aravamudhan, X. Somoulay, C. Lo Giudice, M. A. Poncin, A. C. Dumitru, T. S. Dermody, D. Alsteens, *Nat. Commun.* **2021**, *12*, 2149.
[22] D. Tuckwell, D. A. Calderwood, L. J. Green, M. J. Humphries, *J. Cell Sci.* **1995**, *108*, 1629.
[23] K. Zhang, J. Chen, *Cell Adhes. Migr.* **2012**, *6*, 20.
[24] S. K. Dickeson, J. J. Walsh, S. A. Santoro, *J. Biol. Chem.* **1997**, *272*, 7661.
[25] J. Yang, S. J. L. Petitjean, M. Koehler, Q. Zhang, A. C. Dumitru, W. Chen, S. Derclaye, S. P. Vincent, P. Soumillion, D. Alsteens, *Nat. Commun.* **2020**, *11*, 4541.
[26] D. J. Müller, A. C. Dumitru, C. Lo Giudice, H. E. Gaub, P. Hinterdorfer, G. Hummer, J. J. De Yoreo, Y. F. Dufrêne, D. Alsteens, *Chem. Rev.* **2020**, https://doi.org/10.1021/acs.chemrev.0c00617.
[27] D. Alsteens, R. Newton, R. Schubert, D. Martinez-Martin, M. Delguste, B. Roska, D. J. Müller, *Nat. Nanotechnol.* **2017**, *12*, 177.
[28] M. Delguste, C. Zeippen, B. Machiels, J. Mast, L. Gillet, D. Alsteens, *Sci. Adv.* **2018**, *4*, eaat1273.
[29] M. Koehler, P. Aravamudhan, C. Guzman-Cardozo, A. C. Dumitru, J. Yang, S. Gargiulo, P. Soumillion, T. S. Dermody, D. Alsteens, *Nat. Commun.* **2019**, *10*, 4460.
[30] E. Evans, K. Ritchie, *Biophys. J.* **1997**, *72*, 1541.
[31] E. A. Evans, D. A. Calderwood, *Science* **2007**, *316*, 1148.
[32] E. Evans, P. Williams, presented at *Physics of bio-molecules and cells. Physique des biomolécules et des cellules*, Berlin, Heidelberg, **2002**.
[33] A. Ortega-Esteban, I. Horcas, M. Hernando-Pérez, P. Ares, A. J. Pérez-Berná, C. San Martín, J. L. Carrascosa, P. J. de Pablo, J. Gómez-Herrero, *Ultramicroscopy* **2012**, *114*, 56.
[34] F. E. Fleming, K. L. Graham, Y. Takada, B. S. Coulson, *J. Biol. Chem.* **2011**, *286*, 6165.
[35] J. Dehullu, J. A. Vorholt, P. N. Lipke, Y. F. Dufrêne, *Trends Microbiol.* **2019**, *27*, 728.
[36] V. Reiter-Scherer, J. L. Cuellar-Camacho, S. Bhatia, R. Haag, A. Herrmann, D. Lauster, J. P. Rabe, *Biophys. J.* **2019**, *116*, 1037.
[37] J. Alanko, A. Mai, G. Jacquemet, K. Schauer, R. Kaukonen, M. Saari, B. Goud, J. Ivaska, *Nat. Cell Biol.* **2015**, *17*, 1412.
[38] J. Jokinen, D. J. White, M. Salmela, M. Huhtala, J. Käpylä, K. Sipilä, J. S. Puranen, L. Nissinen, P. Kankaanpää, V. Marjomäki, T. Hyypiä, M. S. Johnson, J. Heino, *EMBO J.* **2010**, *29*, 196.

[39] R. Lima e Silva, Y. Kanan, A. C. Mirando, J. Kim, R. B. Shmueli, V. E. Lorenc, S. D. Fortmann, J. Sciamanna, N. B. Pandey, J. J. Green, A. S. Popel, P. A. Campochiaro, *Sci. Transl. Med.* **2017**, *9*, eaai8030.
[40] R. Tarazona, G. López-Lluch, M. D. Galiani, E. Aguado, F. Barahona, R. Solana, J. Peña, *J. Immunol.* **2000**, *165*, 6776.
[41] N. Heveker, M. Montes, L. Germeroth, A. Amara, A. Trautmann, M. Alizon, J. Schneider-Mergener, *Current Biol.* **1998**, *8*, 369.
[42] R. C. Larue, E. Xing, A. D. Kenney, Y. Zhang, J. A. Tuazon, J. Li, J. S. Yount, P.-K. Li, A. Sharma, *Bioconjugate Chem.* **2021**, *32*, 215.
[43] P. Karoyan, V. Vieillard, L. Gómez-Morales, E. Odile, A. Guihot, C.-E. Luyt, A. Denis, P. Grondin, O. Lequin, *Commun. Biol.* **2021**, *4*, 197.
[44] L. Wildling, B. Unterauer, R. Zhu, A. Rupprecht, T. Haselgrübler, C. Rankl, A. Ebner, D. Vater, P. Pollheimer, E. E. Pohl, P. Hinterdorfer, H. J. Gruber, *Bioconjugate Chem.* **2011**, *22*, 1239.
[45] H. J. Butt, M. Jaschke, *Nanotechnology* **1995**, *6*, 1.